Towards understanding the special stability of $SrCoO_{2.5}$ and $HSrCoO_{2.5}$

Sze-Chun Tsang, Jingzhao Zhang, Kinfai Tse, and Junyi Zhu*
Department of Physics, The Chinese University of Hong Kong, Shatin, New Territories, Hong Kong

(Received 12 June 2018; revised manuscript received 15 October 2018; published 25 February 2019)

Reversible hydrogen incorporation was recently attested [Lu *et al.*, Nature (London) **546**, 124 (2017)] in $SrCoO_{2.5}$, the brownmillerite phase (BM) of strontium cobalt oxide (SCO), opening new avenues in catalysis and energy applications. However, existing theoretical studies of BM-SCO are insufficient, and that of $HSrCoO_{2.5}$, the newly reported hydrogenated SCO (H-SCO) phase, is especially scarce. In this work, we demonstrate how the electron-counting model can be used in understanding the phases, particularly in explaining the stability of the oxygen-vacancy channels, and in examining the Co valance problem. Using density-functional theoretical methods, we analyze the crystalline, electronic, and magnetic structures of BM- and H-SCO. Based on our structure search, we discovered stable phases with large band gaps (>1 eV) for both BM-SCO and H-SCO, agreeing better with experiments on the electronic structures. Our calculations also indicate limited charge transfer from H to O, which may explain the special stability of the H-SCO phase and the reversibility of H incorporation observed in experiments. Contrary to the initial study, our calculations also suggest intrinsic antiferromagnetism of H-SCO, showing how the measured ferromagnetism has possible roots in hole doping.

DOI: 10.1103/PhysRevMaterials.3.024603

I. INTRODUCTION

In 2017, reversible hydrogen incorporation and three-phase interconversion was realized [1] in the brownmillerite (BM) phase of strontium cobalt oxide (SCO, or strontium cobaltite), of a chemical formula $SrCoO_{2.5}$, via ionic-liquid gating, and a new, hydrogenated phase of SCO (H-SCO, formula $HSrCoO_{2.5}$) was discovered. Due to its exceptionally robust oxygen-vacancy channels (OVCs) which facilitate ionic transport, incorporation, and extraction, BM-SCO has promising prospects in fuel cell technology, energy storage, and catalysis. Such breakthrough in the study and manipulation of magnetic complex oxides is also highly encouraging towards ongoing research in the field.

Illustration of the two phases are provided in the form of Fig. 1, with the structures available in the `.cif` format in the Supplemental Material (SM) for the interested reader [2]. To distinguish between the various cobalt (Co) and oxygen (O) sites, we named the Co centers according to their coordination numbers ($Co_{(6)}$ is six coordinated, etc.), and the O sites according to the metallic sites they are approximately coplanar with [$O_{(6)}$ for $Co_{(6)}$, $O_{(Sr)}$ for strontium (Sr), etc.].

For the further engineering of SCO, especially for fuel cell applications, insights in both the actively researched BM-SCO, and the novel and barely researched H-SCO phases, are indispensable. However, some fundamental issues remain unresolved.

First, there are uncertainties regarding their ground-state crystalline, electronic, and magnetic structures. Though it has been experimentally [3] and numerically [4,5] established that BM-SCO has a G-type antiferromagnetic (AFM) and semiconducting ground state, with a crystallographic space-group symmetry variously described as *Ima*2 [5,6] or *Imma* [7], it must be noted that a definite value of the band gap has not been provided in literature, with discrepancies among the calculated and measured values (Table I). This problem is likely to be aggravated by the experimental conditions, the electronic environment (such as the ionic-liquid gating employed in [1]), the presence of defects, secondary phases, and different local configurations, as well as the variance in the actual optical transitions measured.

Even less well understood is the H-SCO phase. The initial study [1] indicates a semiconductor with a wider band gap relative to BM-SCO, exhibiting weak ferromagnetism (FM); however, the presented numerical evidence was insufficient towards confirming the experimental observations. Moreover, the measured FM is counterintuitive according to the superexchange picture, which for an overwhelming majority of magnetic oxide semiconductors predicts intrinsically AFM couplings; the possibility exists that the experimentally observed FM was carrier mediated and could be attributed to dopants and defects, as is usual for FM in semiconductors [10,11]. Indeed, a comparison between the two magnetic couplings would have been instructive towards resolving this difficulty, but was wanting. Also, properly characterizing the ground-state configuration is a prerequisite for further investigations into diffusion mechanisms in H-SCO, which are invaluable towards potential device applications.

Another issue is the robustness of the OVCs. In semiconductors, vacancies are often disordered, and have positive formation energies [12–14]. However, the oxygen-deficient BM-SCO phase is variously attested as stable or metastable [8,15,16] with respect to oxidation to the fully oxygenated and perovskite-structured SCO (P-SCO, formula $SrCoO_3$). Furthermore, the OVCs in BM-SCO are arranged in a parallel manner consistent with the aforementioned symmetries, which define its highly directional [17] ionic transport [18]

*Corresponding author: jyzhu@phy.cuhk.edu.hk

 ©2019 American Physical Society

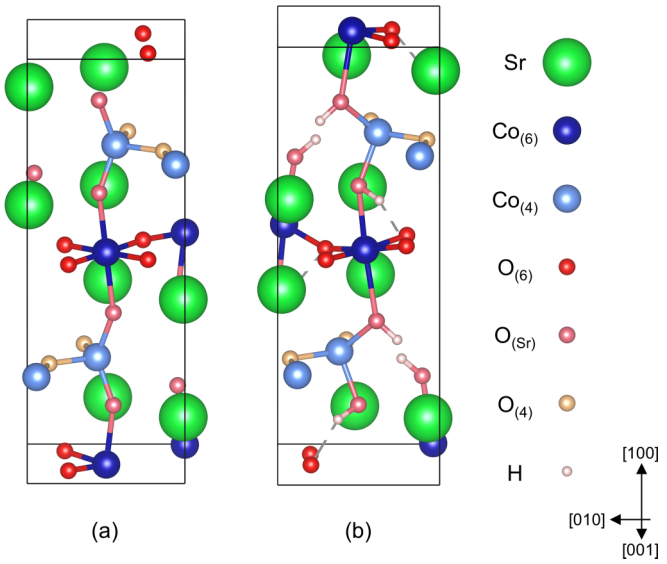

FIG. 1. Illustrations of the (a) BM-SCO and (b) H-SCO phases; the different Co and O sites are color coded here for illustrative purpose.

and catalytic [9,19] properties. The importance of such robust OVCs towards applications is self-obvious, but the physical origin of this stability is yet unclear.

In view of the promising prospect of BM-SCO (and, by extension, H-SCO), and the aforementioned issues surrounding the phases, we set out to revisit the basic problem of their stabilities. *Qualitatively*, the electron-counting model (ECM) [20], widely used in the investigations of surface reconstructions and in stability analyses of semiconducting surface states, may offer insights towards our problem. Such models and insights can then be *quantitatively* verified by density-functional theoretical (DFT) calculations, which allow for the determination of the ground state of the SCO phases, and subsequently their electronic structures.

II. ELECTRON-COUNTING MODELS

To the best of our knowledge, the application of the ECM formalism to the analysis of defects or defect complexes, which the OVCs are, is previously unheard of. However, since the OVCs of BM-SCO (and H-SCO) can be considered as specially aligned inner surfaces, they should also in principle satisfy ECM. Now, the key to ECM is the fulfilling of the octet rule around atoms by coordination, where a fractional number of electrons in each of such assumed "coordinate bonds" (hereafter called "bonds," but not in the strict chemical sense) is permitted; previously, similar treatment has been proposed in the ECM investigation of TiO_2 [21].

TABLE I. Comparison of some attested band gap values in BM-SCO.

Reference	Study type	Band gap (eV)	Notes
Pardo *et al.* [4]	Numerical	0.69[a]	$U - J = 4$ eV[b]
Muñoz *et al.* [5]	Numerical	0.63[a]	[b]
Lu *et al.* [1]	Numerical	0.25[a]	$U - J = 4$ eV[b]
Liang *et al.* [6]	Numerical	1.4	$U - J = 6.5$ eV[b]
Choi *et al.* [8]	Experimental	0.35	
Saib *et al.* [9]	Experimental	1.10	
Lu *et al.* [1]	Experimental	2.12	

[a]Estimated from the densities of states (DOSs).
[b]Generalized-gradient approximation (GGA) with on-site Coulomb interaction ($+U$).

We proceed to show that BM-SCO [Fig. 1(a)] satisfies ECM, with the following simplifying assumptions. First, we assume that both types of Co centers, irrespective of their local electronic environments, have six surrounding "lobes" of charge distributions. This assumption suggests that the four-coordinated or "tetrahedral" Co center ($Co_{(4)}$) can be considered as a distorted "octahedral" (i.e., six-coordinated) center ($Co_{(6)}$), with two dangling bonds in lieu of the missing O atoms. We also note the average valence of Co to be three, justified by balancing the formal oxidation states of the elements per chemical formula of BM-SCO; therefore, a Co atom contributes 3/6 electron to each Co–O bond.

Since ECM requires dangling bonds on the cationic centers to be empty [20], for each $Co_{(4)}$ center, a surplus of one electron is incurred. As for each O atom, invariably bonded to two Co centers regardless of its site, it gains in total one electron from the two bonds beside its six valence electrons—still one electron short of an octet.

With the above discussion, and noting how $Co_{(6)}$ and $Co_{(4)}$ centers are equal in concentration, we examine the electronic surplus per formula of BM-SCO ($SrCoO_{2.5}$) and show electronic balance to indeed be achieved, hence stabilizing the OVCs:

$$\underbrace{1\times(+2)}_{\mathrm{Sr}}+\underbrace{0.5\times(0)}_{\mathrm{Co_{(6)}}}+\underbrace{0.5\times(+1)}_{\mathrm{Co_{(4)}}}+\underbrace{2.5\times(-1)}_{\mathrm{O}}=0. \quad (1)$$

As for H-SCO [Fig. 1(b)], we can consider two possibilities in assigning a charge state to hydrogen (H), which is known to assume different charge states even in the same material, such as Si [22], the determination of which is often a point of contention. The first possibility is that H is considered nil-valent, equivalent to the weak-O–H bonds limit. This makes the phase very much like BM-SCO, only with H incorporated via physisorption. The charge transfers and valence changes, if any, would be small in this case, in essence preserving the BM-SCO ECM above.

The other possibility is that H is taken to be monovalent, with strong O–H bonds; this essentially results in a charge transfer to the $O_{(Sr)}$ atoms, to which H atoms are bonded. To simplify matters, we just take H as an electron donor [6], like Sr. Assume for a moment a Co valence of v. Each Co–O bond thus consists of $v/6$ electron from Co and $(8-v)/6$ electron from O, amounting to an excess of $v/3$ electron per $Co_{(4)}$. Each O has an electron deficiency of $8-6-2\cdot v/6 = (6-v)/3$; thus to strike electronic balance, this equality needs to be satisfied:

$$\underbrace{1\times(+1)}_{\mathrm{H}}+\underbrace{1\times(+2)}_{\mathrm{Sr}}+\underbrace{0.5\times(0)}_{\mathrm{Co_{(6)}}}+\underbrace{0.5\times\left(\frac{v}{3}\right)}_{\mathrm{Co_{(4)}}}+\underbrace{2.5\times\left(\frac{v-6}{3}\right)}_{\mathrm{O}}=0. \quad (2)$$

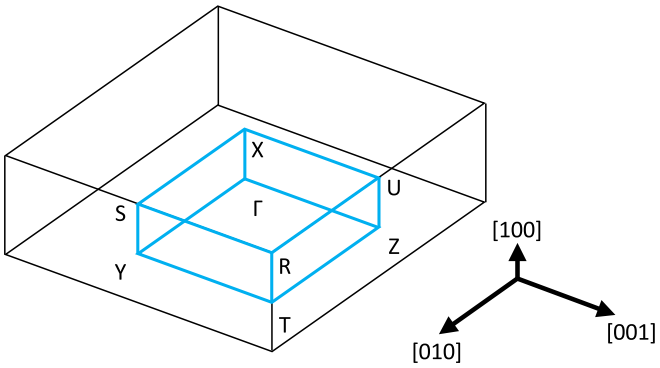

FIG. 2. Schematics of the first BZ (in thin lines) and the IBZ (in thicker lines) of the BM-SCO and H-SCO phases, with the high-symmetry points labeled.

Hence we have $v = 2$, meaning that the charge transfer induces a valence change in Co from (III) to (II), consistent with previous proposals [1,23]; which of the pictures is more descriptive of H-SCO remains to be verified by calculations.

III. COMPUTATIONAL DETAILS

A. General methodology

The Vienna *ab-initio* simulation package (VASP) [24,25] was used to perform all calculations. Spin-polarized calculations were done using the Perdew-Burke-Ernzerhof formulation of the generalized-gradient approximation (PBE-GGA) [26], with pseudopotentials (PPs) generated by the projector augmented-wave (PAW) [27,28] method. A G-type spin texture was assumed for AFM calculations. Plane-wave bases were truncated to a 400 eV energy cutoff, and gamma-centered k-point meshes were used to sample the reciprocal space. All lattice-vector, positional, and electronic degrees of freedom were relaxed, with forces on individual atoms converged to under 0.02 eV/Å. For atomic charge [magnetic moment (MM)] analyses, the integrated site- and orbital-projected charge (spin) density around each atom was found by the PAW-based quick projection scheme as implemented in VASP.

Simulation cells were constructed based on a fully relaxed 36-atom BM-SCO primitive cell, similar to the cell of *Ima*2 symmetry described by Muñoz *et al.* [5]. (It should be noted that the reported G-type AFM necessitated the doubling of the primitive cell.) Single-H adsorption was studied using a 144-atom $1 \times 2 \times 2$ BM-SCO host supercell. The k-point meshes used for primitive-cell and supercell calculations were $2 \times 5 \times 5$ and $2 \times 3 \times 3$, respectively; after full relaxations, band structures were calculated by sampling k-points along the twelve edges of the irreducible Brillouin zone (IBZ) (Fig. 2) of the orthogonal primitive cell. The k-point mesh size, and the plane-wave energy cutoff, were convergence tested to ensure the physicality of the results.

The effects of correlation between Co-d electrons were included by considering the on-site Coulomb interaction (U), utilizing the simplified, rotationally invariant Hubbard model [29] by Dudarev *et al.* [30], where the Coulomb U and the exchange J parameters enter the Hamiltonian via only their difference $U - J$, which we simplified to U by choosing $J = 0$. After extensive tests (see Sec. III B), we settled on choosing $U = 4$ eV, in keeping with previous practice in BM-SCO calculations [1,5].

B. U and functional testing

Seeing how H-SCO and BM-SCO should be *a priori* treated as distinct materials, and established parameters which work for BM-SCO may be suboptimal for H-SCO, we conducted tests on the structural, electronic, and magnetic properties of H-SCO, with respect to the choice of exchange–correlation functionals and U parameters. Based on the configuration reported in [1], we constructed a symmetrized H-SCO unit cell [Fig. 1(b)], which we then relaxed using the local-density-approximation (LDA) and PBE-GGA functionals, in conjunction with their corresponding PP sets, with the U parameter set between zero and 5 eV.

The trend for the band gap energy is consistent across both functionals (Fig. 3) that it increases with increasing U and, for LDA, the gap closes when U is small. In view of the prominent Co-d character of the valence and conduction bands of BM-SCO [5], we would expect the situation to be somewhat similar in H-SCO. Since the Hubbard U term adjusts the strength of the on-site Coulomb interaction between Co-d electrons, the band edges (and thus the band gap energy) are naturally highly dependent on it. Due to the loss of the band gap with LDA at small U, we deemed such settings to be unsuitable for the description of H-SCO, although they gave good agreement to the crystalline structure (SM, Fig. 2) [2].

We also tested for the magnetic coupling energy $\Delta F_{\mathrm{AFM-FM}}/N_{\mathrm{Co}}$, i.e., the free energy difference per Co atom between the AFM and FM phases, to check the energetic favorability of the two couplings. To our surprise, AFM was found to be energetically favorable relative to FM,

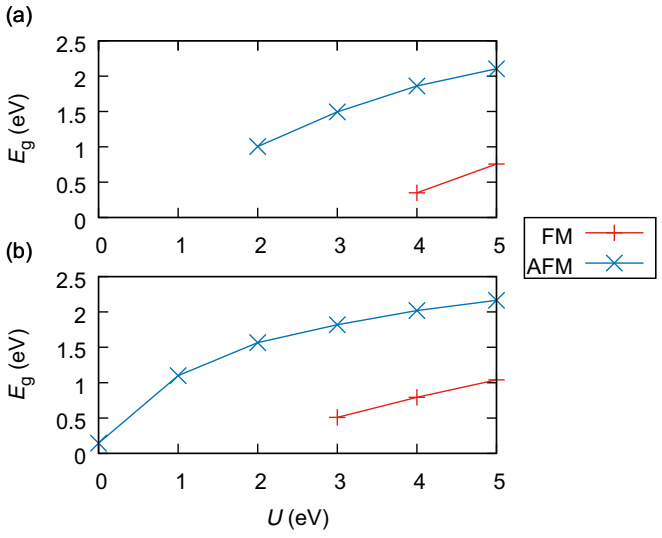

FIG. 3. Plots of the band gap energy E_g of H-SCO, if any, against the U parameter, for the (a) LDA and (b) PBE-GGA functionals; band gaps estimated from the eigenvalues of the highest-occupied and lowest-unoccupied bands on the $2 \times 5 \times 5$ k-point mesh.

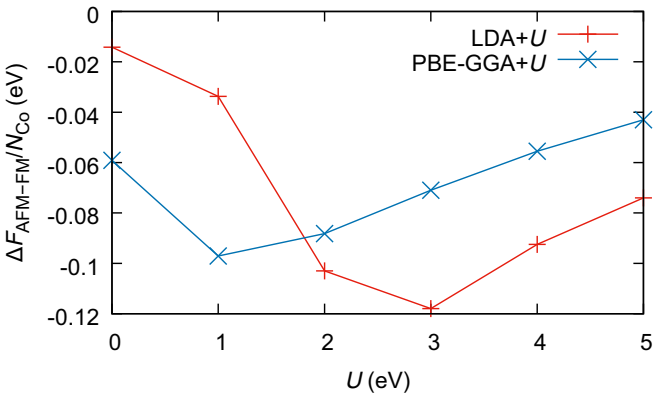

FIG. 4. Plot of the magnetic coupling energy $\Delta F_{\mathrm{AFM-FM}}/N_{\mathrm{Co}}$ of H-SCO against the U parameter, for both the LDA and PBE-GGA functionals.

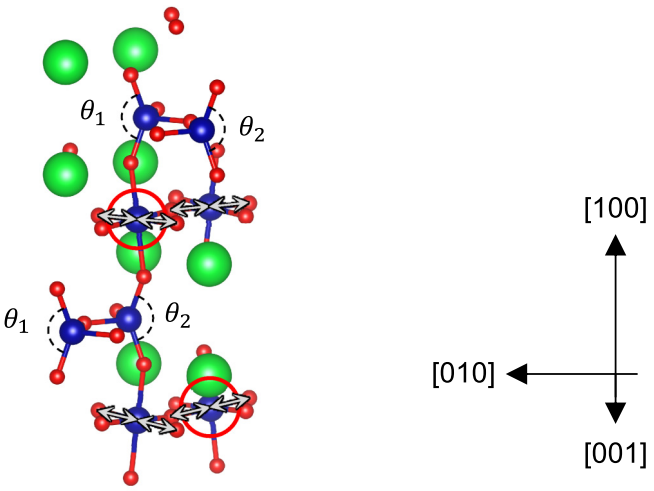

FIG. 5. Illustration of the distribution of the longer $\mathrm{Co_{(6)}}$–$\mathrm{O_{(6)}}$ bonds (overlaid with gray arrows) in *phase-1* BM-SCO; note how the bond arrangements about the two circled $\mathrm{Co_{(6)}}$ centers, $(\frac{1}{2}, \frac{1}{2}, \frac{1}{2})$ apart in direct coordinates, are different. Also shown: definitions of the $\mathrm{O_{(Sr)}}$–$\mathrm{Co_{(4)}}$–$\mathrm{O_{(Sr)}}$ bond angles θ_1 and θ_2.

consistently for both functionals (Fig. 4) at all tested values of U, in apparent contradiction to the experimental observation in [1].

IV. RESULTS AND DISCUSSIONS

See SM [2] for band-component analyses (Sec. IV, SM) and `.cif` files (Sec. V, SM) of the three discussed BM-SCO structures, namely, *phases 1–3*, and that of the lowest-energy H-SCO structure.

A. Brownmillerite phase

A BM-SCO cell was first obtained after detailed structure optimization. The most stable structure we obtained, hereafter referred to as *phase 1*, retains from the *Ima*2 space group the reflectional symmetry about the OVCs, and the 2_1 screw axes along them. However, a split among the $\mathrm{Co_{(6)}}$–$\mathrm{O_{(6)}}$ bond lengths to 2.052(4) Å and 1.84660(8) Å eliminates the translational symmetry between the two planes of $\mathrm{Co_{(6)}}$ (Fig. 5), thus lowering the symmetry to a shifted $Pmc2_1$. It has large direct band gaps of 1.37 eV (Table II) at the Y and S points [Fig. 6(a)], with the valence and conduction bands (VB and CB, respectively) governed by the coupling between Co-3*d* and O-2*p* orbitals (SM, Fig. 8) [2].

In addition to this most-stable *phase 1*, we also obtained an almost-orthorhombic ($90^\circ < \alpha < 90.1^\circ$) phase with a relatively small gap, which we named *phase 2*; this phase is 123 meV higher in energy compared to *phase 1* for each formula of $SrCoO_{2.5}$. The band gap energy also decreases to 0.67 eV, with the CB minimum (CBM) shifting to the Γ point [Fig. 6(b)]. [Note that as an approximation, the reciprocal space of *phase-2* BM-SCO is traversed (Fig. 2) as if the cell is orthorhombic.] Beside the unit-cell distortion, some other geometric differences between these two structures are noted, mainly in the $\mathrm{O_{(Sr)}}$–$\mathrm{Co_{(4)}}$–$\mathrm{O_{(Sr)}}$ bond angles (Fig. 5): in *phase 1*, the angles $\theta_1 \approx \theta_2 \approx 139^\circ$, while for *phase 2*, $\theta_1 \approx 141^\circ$ and $\theta_2 \approx 138^\circ$, breaking the 2_1-screw axis symmetry along the OVCs. Such local structural distortions induce the decrease of the $\mathrm{Co_{(4)}}$ MMs (Table II), creating also a predominantly $\mathrm{Co_{(4)}}$–$\mathrm{O_{(Sr)}}$ gap state [SM, Figs. 9(b) and 9(e)] [2], causing a smaller overall band gap; intuitively, the *p–d* couplings are changed upon the symmetry breaking.

As a control, another orthorhombic phase, *phase 3*, was obtained by relaxation under a forced *Ima*2 [5] symmetry. Despite the minute differences in the lattice parameters

TABLE II. Comparison of the three obtained BM-SCO phases, with *phases 1*, *2*, and *3* being $Pmc2_1$ orthorhombic, slightly monoclinic, and *Ima*2 orthorhombic, respectively.

Property	*Phase 1*	*Phase 2*	*Phase 3*
Lattice constants a, b, c (Å)	15.589, 5.570, 5.438	15.636, 5.334, 5.440[a]	15.529, 5.601, 5.401
$\mathrm{O_{(Sr)}}$–$\mathrm{Co_{(4)}}$–$\mathrm{O_{(Sr)}}$ angle θ_1	139°	138°	126°
$\mathrm{O_{(Sr)}}$–$\mathrm{Co_{(4)}}$–$\mathrm{O_{(Sr)}}$ angle θ_2	139°	141°	126°
Relative free energy ΔF per formula (eV)	0	+0.123	+0.0368
$\mathrm{Co_{(6)}}$ MM (μ_B)	2.959	2.971(2)	2.958
$\mathrm{Co_{(4)}}$ MM (μ_B)	2.915	2.4(5)	2.907(1)
Band gap energy (eV), nature	1.37, direct	0.67, indirect	0.93 (estimate)[b]

[a]Indexed with reference to the *phase-1* cell.
[b]Estimated from the eigenvalues sampled on the k-point mesh.

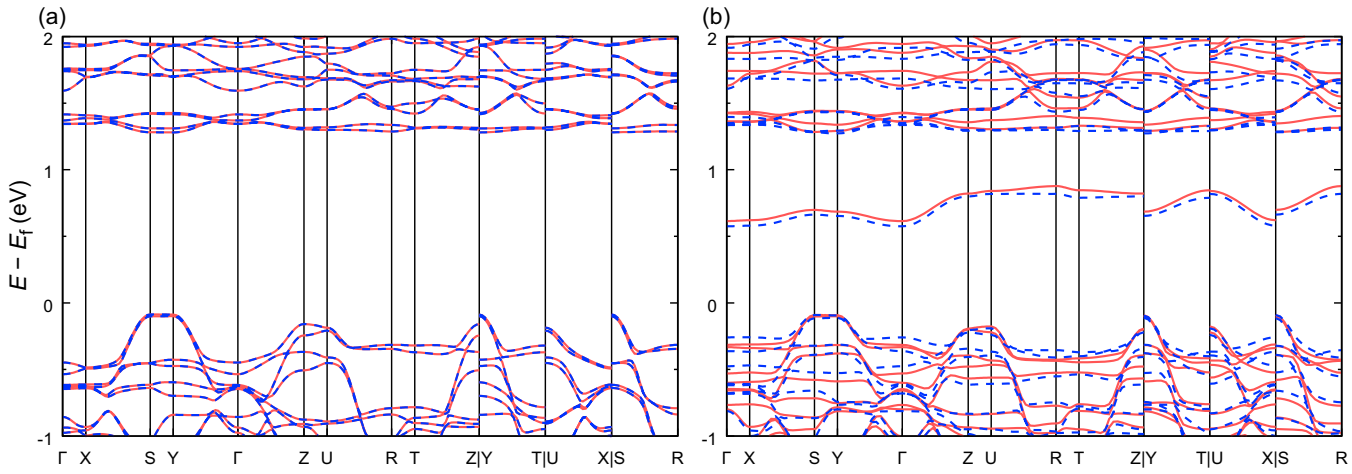

FIG. 6. Plots of the band structures of (a) *phase-1* and (b) *phase-2* BM-SCO near the band edges, with spin-up (-down) bands in red (color)/light gray (gray scale) solid lines [blue (color)/dark gray (gray scale) dotted lines].

(Table II), the band gap width decreases to 0.93 eV; the structure is also 36.8 meV per formula of BM-SCO higher in energy than *phase 1*. Moreover, our phonon calculations [2] also indicate the dynamical instability of this *Ima*2 phase with respect to the $Pmc2_1$ *phase 1*. As the difference in space groups arises from the differing Co–O bond lengths on the octahedral layer (Fig. 5), the spontaneous and energetically favorable symmetry breaking in going from *phase 3* to *phase 1* can be seen as a manifestation of the Jahn-Teller effect [31,32].

The above results also suggest how sensitive the electronic and magnetic properties of BM-SCO are to the local structures, especially near the OVC; the phases, which can all be considered perturbations to a predominantly *Ima*2 symmetry, may easily interconvert due to thermal fluctuations at typical working temperatures of solid oxide fuel cells (SOFCs), which are in the order of 10^2 to 10^3 K [33]. This may also explain why previous theoretical studies predicted small band gaps, inconsistent with recent experiments (Table I).

B. Hydrogenated phase

1. Lowest-energy configuration

To gain insights towards the construction of a low-energy H-SCO phase, we first examined the preferred adsorption sites at the dilute limit. A single H atom was introduced to the large ($1 \times 2 \times 2$) BM-SCO supercell at different possible adsorption sites, which are listed in Fig. 7 along with their relative free energies. The most energetically favorable configuration, "$O_{(Sr)}$–$O_{(6)}$ away" [Fig. 7(a)], has the H atom bonded to an $O_{(Sr)}$, pointing *away* from the OVC towards a nearby $O_{(6)}$. This differs from earlier studies [1,6] suggesting the relative stability of the "$O_{(Sr)}$–$O_{(4)}$-across" configuration [Fig. 7(f)] at the dilute limit, which we found to be marginally less favorable energetically by 40 meV; relative to the "adsorption–coordination site" (e.g., $O_{(6)}$ [Figs. 7(b) and 7(c)], $O_{(Sr)}$ [Figs. 7(a) and 7(f)], and between metal ions [Figs. 7(g) and 7(h)]) on which the H atom settle, its orientation would seem to exert a much smaller effect on the energy.

Other configurations, like having the H atom directly adjacent to a Co site, were also sampled, but they were unfeasible and eventually converged to the listed ones. Still, we do note that it is almost impossible to exhaust all the possible configurations, given the multitudes of adsorption sites and H orientations, even when we only considered the single-H cases; analysis of the intermediate-hydrogenation regime would be notedly [6] and prohibitively difficult.

As discussed in Sec. III, SM [2], we have shown the single-H states to be semiconducting and localized, which suggests the generality of the stable local configurations of adsorbed H atoms, and their relevance even at elevated H concentrations. Hence, based on the single-H results, we then proceeded to construct fully hydrogenated H-SCO unit cells by putting H atoms onto $O_{(Sr)}$, which is the preferred site at the dilute limit, when also ideally preserving the *Ima*2-like symmetry of BM-SCO. Among the tested configurations (Fig. 8), "($O_{(Sr)}$–$O_{(4)}$-across)+($O_{(Sr)}$–$O_{(6)}$-away, $+c$)" [Fig. 8(c)], i.e., that which was constructed for the functional and U-parameter tests [Fig. 1(b)], has the lowest energy. This configuration has H orientations arranged highly symmetrically, with half the H pointing *across* the OVCs to opposing $O_{(4)}$, and half towards $O_{(6)}$ pointing *away* from the OVCs, in the $+c$ direction relative to the adsorbing $O_{(Sr)}$, essentially mixing the lowest-energy single-H configurations reported in previous investigations [1,6] and ours in equal proportions. Such is identical to the upper channel in the configuration presented in [1], which we also attempted to replicate; however, it settled into the "($O_{(Sr)}$–$O_{(4)}$-across)+($O_{(Sr)}$–$O_{(6)}$-away, $+c$)+($O_{(Sr)}$-along)" configuration [Fig. 8(e)], qualitatively differing from the lowest-energy configuration [Fig. 8(c)] only by turning one of the four H atoms in the "$O_{(Sr)}$–$O_{(4)}$-across" orientation such that it now points *along* the OVC. This break of symmetry is however energetically unfavorable by a moderate margin of 24 meV per formula.

Other configurations were formed by orienting the $O_{(Sr)}$−H bonds towards different $O_{(6)}$ atoms [Figs. 8(a) and 8(b)], such that the O–H bonds point *towards* [Fig. 8(a)] or *away* from [Fig. 8(b)] the OVCs, in the $-c$ direction; these are found to incur considerable energy penalties. Intriguingly,

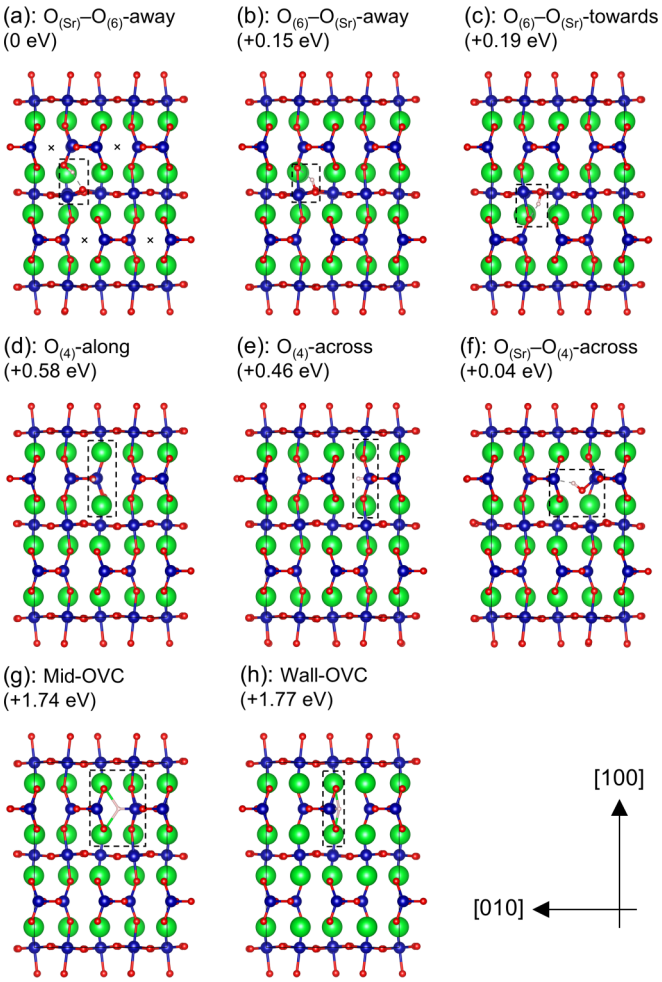

FIG. 7. Single-H adsorption sites, viewed along the [00$\bar{1}$] direction; adsorbed H and surrounding atoms boxed as visual aid. Relative free energies ΔF of the $1 \times 2 \times 2$ supercells are also listed above each figure. OVCs are marked with crosses in (a).

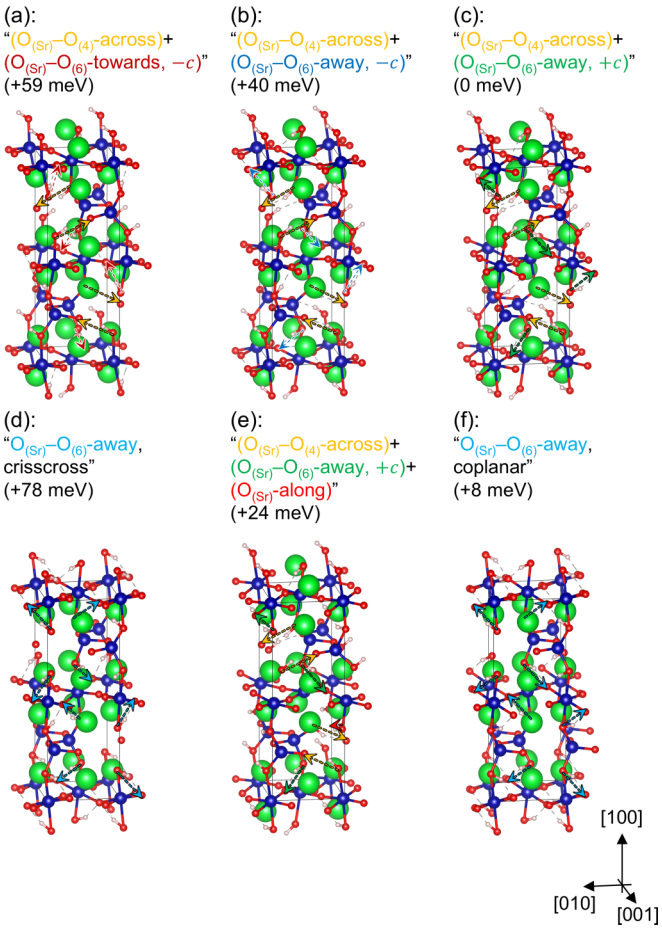

FIG. 8. Fully hydrogenated H-SCO primitive cells and their relative free energies ΔF per formula of $HSrCoO_{2.5}$. The eight arrows in each subfigure indicate the approximate orientations of the $O_{(Sr)}$–H bonds.

pointing all O–H bonds *away* from the OVCs [Fig. 8(d)] like the single-H favored case [Fig. 7(a)] in a *crisscross* manner turns out to be very energetically unfavorable, unless one aligns all O–H bonds to be *coplanar* along the (011) plane [Fig. 8(f)], inducing a shrink along said diagonal upon cell relaxation and resulting in a monoclinic cell with $\alpha \approx 84^\circ$, which is relatively low in energy. This is reminiscent of the polymorphism of crystal symmetries found in perovskites [34], to which brownmillerites (of which H-SCO is a derivative) are closely related.

2. *Structural, electronic, and magnetic properties*

The lattice constants a, b, and c in the obtained H-SCO phase increase to 16.064 Å, 5.727 Å, and 5.626 Å, respectively, indicating lattice expansion relative to BM-SCO due to hydrogen incorporation. The primitive cell exhibits a shifted $Pna2_1$ symmetry, preserving the 2_1 screw axes of the brownmillerite structure along the OVCs and the glide planes (100) and (200) of the idealized $Ima2$ cell, at the cost of the reflection symmetry of the OVCs about the $Co_{(4)}$–$O_{(4)}$ planes. This is in contrast with the $Pmc2_1$ BM-SCO cells, where the glide planes are lost instead. Indeed, the change of space groups upon hydrogenation is not unheard of; as a more drastic example, hydrogen-doping proves effective in stabilizing the zinc-blende phase against the wurtzite phase in, for example, zinc oxide and gallium nitride [35].

The change in the electronic structure (Fig. 9) relative to the BM-SCO phase is drastic. H-SCO has a band gap 1.99 eV wide, 620 meV wider than that of BM-SCO, in qualitative agreement with previous results [1] that the band gap widened by 720 meV upon hydrogenation. Like in BM-SCO, the valence and conduction bands are still heavy in Co-3d and O-2p characters, yet complications arise: the CBM is now shifted to the Γ point, acquiring a somewhat s–d character (SM, Fig. 10) [2]. Compared to the BM-SCO CBM, which is of p–d character, the band curvature is much increased, suggesting enhanced carrier mobility when the system is lightly electron doped.

As mentioned in Sec. III B, in seeming contradiction with the experimentally reported FM [1], the G-type AFM in BM-SCO is preserved, and is stabilized against FM by

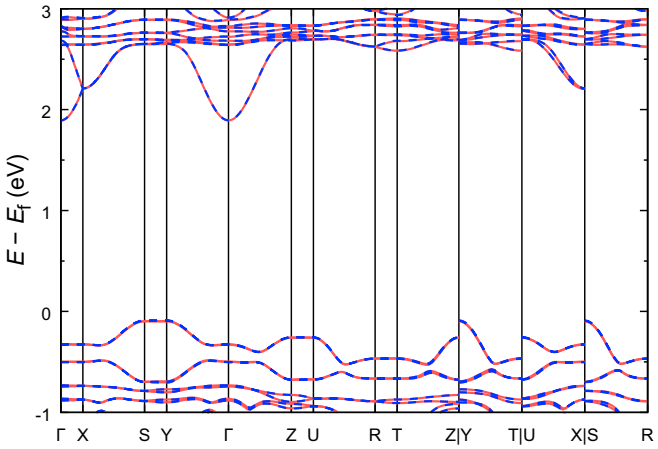

FIG. 9. Plot of the band structure of H-SCO near the band edges, with spin-up (-down) bands in red (color)/light gray (gray scale) solid lines [blue (color)/dark gray (gray scale) dotted lines].

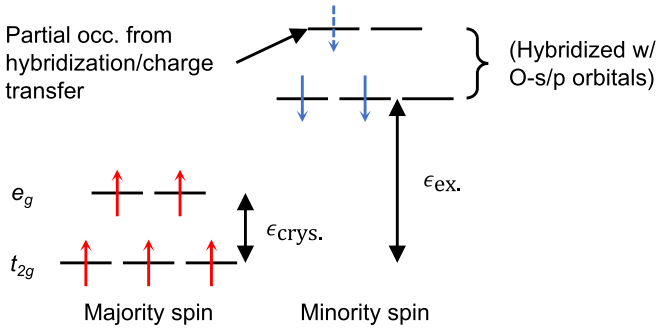

FIG. 10. Schematics of the energy splitting of the Co-d orbitals.

56 meV per Co atom. The finding is also qualitatively supported by hybrid and meta-GGA DFT results (Sec. I C, SM) [2]. This apparent inconsistency, as we will later address in Sec. IV C, may possibly be attributed to hole-mediated FM in the experimental sample. The MMs on $Co_{(6)}$ and $Co_{(4)}$ become $2.627\mu_B$ and $2.647\mu_B$, respectively, about $0.3\mu_B$ lower compared to those in BM-SCO.

From Table III, it is seen that the projected charge and MMs of the Co-d orbitals are qualitatively similar, consistent with our ECM, where $Co_{(6)}$ and $Co_{(4)}$ centers are treated as having the same valence, and identical up to the number of O ligands. We hereby give a simplistic argument towards the Co MM, in terms of the atomic orbital couplings; we begin by considering BM-SCO. Assume for Co a d^7 configuration (Fig. 10). Considering the assumed O_H symmetry of a Co center, the e_g (d_{z^2}, $d_{x^2-y^2}$) orbitals are split upwards relative to the t_{2g} (d_{xy}, d_{yz}, d_{zx}) orbitals by the crystal field. With sufficiently large exchange splitting ϵ_{ex} between the spins, relative to the crystal-field splitting ϵ_{crys}, the five majority-spin states would be fully occupied, and the remaining electrons occupy two of the minority-spin t_{2g} states.

Now, we consider the hopping of electrons between the Co and O orbitals, as described in the tight-binding and Hubbard [29] models. For convenience, we align the z axis along the Co–O "bond." By symmetry arguments, we see that the Co-d_{z^2} (i.e., e_g) and O-p_z (or O-s) orbitals directly overlap, allowing the electrons to easily hop between the orbitals. (This is, in the hybridization language, σ bonding.) Less direct yet still permitted is hopping (i.e., π bonding) between the Co-d_{xy} (i.e., t_{2g}) and O-p_x orbitals, and the Co-d_{yz} and O-p_y orbitals. This creates further splitting among the Co-d states, partially populating the minority-spin Co-d levels with electrons which hopped from O, thus contributing to a d-orbital MM of slightly less than three.

TABLE III. Select orbital projections of the charges and magnetic moments around various species in BM-SCO and H-SCO.

	Charge (elem. charge)		MM (μ_B)	
Orbital	BM-SCO	H-SCO	BM-SCO	H-SCO
$Co_{(6)}$-d	6.982	7.173	2.955	2.6055(5)
$Co_{(4)}$-d	7.0865(5)	7.1695(5)	2.863	2.591
$O_{(Sr)}$-d	3.439	3.555(8)	0.1595(5)	0.022(4)
H-s	N/A	0.606(3)	N/A	0.0005(5)

As for H-SCO, it is seen that the O–H bond strength is at a delicate balance which gives rise to the interesting and useful properties of H-SCO seen experimentally. Around H atoms, the charge is qualitatively close to unity (≈0.6 elem. charge) (Table III), and the increase of that around $O_{(Sr)}$ is small (≈0.1 elem. charge) compared to the $O_{(Sr)}$ charge in BM-SCO. This indicates a weak charge transfer from H to $O_{(Sr)}$, evident of physisorption of H in a BM-SCO scaffold, corresponding to the proposed weakly bonded ECM (rf. Sec. II). However, we also note the charge in the Co-d orbitals to increase somewhat (≈0.1 elem. charge), hinting at H−$O_{(Sr)}$−Co hopping of the partially transferred charge, which is qualitatively consistent with the slight decrease ($\approx 0.3\mu_B$) in the Co-d MMs. By virtue of this small increase in the occupation of the hopping-allowed Co-d orbitals by H-s electrons, hydrogenation suppresses the Co-d-to-O-p coupling as previously suggested [1], which affects the energy splitting and ordering of the bands, resulting in the exposure of the new CBM of increased s–d character (SM, Fig. 10) [2]. Such suppressed p–d coupling is consistent with the increase in the charge density around Co, and decreases in Co valence and magnetization, corresponding to the strongly bonded ECM proposed towards the end of Sec. II. As such, H-SCO is best considered to be at the middle ground between the two pictures, indicating intermediate strength of the $O_{(Sr)}$−H bonds, which explains the observed stability of the H-SCO phase, and the reversibility [1] of the H-SCO and BM-SCO interconversion. This suggests high mobility of H in SCO, which would be invaluable towards energetic and catalytic applications.

C. Carrier-mediated magnetism

Finally, we proceed to present a proof of concept showing how the measured weak FM in H-SCO [1] could have been caused by holes. As a demonstration, we calculated the FM and AFM cell free energies after the introduction of a hole

TABLE IV. Table of relative cell free energies ΔF under different spin textures and number change of electrons ΔN_e.

ΔN_e	F_{FM} (eV)	F_{AFM} (eV)
0 (charge-neutral)	+0.44	0
+1 (electron-doped)	+6.09	+5.84
−1 (hole-doped)	−3.56	−3.38

and an electron, holding the lattice vectors constant to better capture the dilute-limit behavior.

As is evident from Table IV, FM is favored upon the introduction of holes, in contrast to the charge-neutral case, whereas AFM is favored when the system is electron doped, as with the neutral case. This is consistent with the band coupling-model picture of charge carrier-mediated FM proposed by Dalpian and Wei [36]. In a real-life scenario, such holes could easily have been introduced by lattice defects and/or dopants (e.g., stray ions), which is almost inevitable in the liquid ion-gated environment employed in [1]. Further numerical investigation of point defects in H-SCO would be instructive towards the understanding of the observed FM.

We also note the possibility of asymmetric (or Dzyaloshinsky-Moriya) [37,38] interaction-mediated effects, which often give rise to weak measured FM in otherwise predominantly AFM systems; however, evaluation of such interaction would require a full noncollinear treatment of the electron spins, which is beyond the scope of this investigation.

V. CONCLUSIONS

By a combination of DFT+U investigation, ECM, and Hubbard model-based arguments, we have analyzed the structural, electronic, and magnetic properties of BM-SCO and H-SCO. Such a study is fundamental for and instrumental towards the further refinement, tuning, and application of the SCO system, which has already shown promising prospects.

Moreover, by the treatment of the OVCs in SCO, which are line defects, as inner surfaces, we have successfully applied ECM to a defect complex in the material bulk. This may open up a new perspective towards the understanding of new materials with similar features.

Particularly, we have shown H-SCO to be an interesting material in its own right, owing to the moderate bonding strength of the incorporated hydrogen, and the increased band gap energy and conduction electron mobility. This may even suggest an entirely new dimension towards the search and development of new classes of materials, with incorporated hydrogen as a useful tuning parameter, both electronically and magnetically.

ACKNOWLEDGMENTS

We thank P. Yu for his insightful input throughout the research process. We also thank the University Grants Committee of Hong Kong for their Early Career Scheme grant (No. 24300814), the Research Grants Council of Hong Kong for their General Research Fund grant (No. 14307018), and The Chinese University of Hong Kong for their direct grant (No. 4053084), all in partial support of this study.

[1] N. Lu, P. Zhang, Q. Zhang, R. Qiao, Q. He, H.-B. Li, Y. Wang, J. Guo, D. Zhang, Z. Duan, Z. Li, M. Wang, S. Yang, M. Yan, E. Arenholz, S. Zhou, W. Yang, L. Gu, C.-W. Nan, J. Wu, Y. Tokura, and P. Yu, Nature (London) **546**, 124 (2017).

[2] See Supplemental Material at http://link.aps.org/supplemental/10.1103/PhysRevMaterials.3.024603 for additional results on functional and U value tests, phonon calculations on the BM-SCO phases, notes on the single-hydrogen BM-SCO configurations, band-component analyses of the BM-SCO and H-SCO phases, and `.cif` files of the structures.

[3] T. Takeda, Y. Yamaguchi, and H. Watanabe, J. Phys. Soc. Jpn. **33**, 970 (1972).

[4] V. Pardo, P. M. Botta, D. Baldomir, J. Rivas, A. Piñeiro, C. de la Calle, J. A. Alonso, and J. E. Arias, Physica B **403**, 1636 (2008).

[5] A. Muñoz, C. de la Calle, J. A. Alonso, P. M. Botta, V. Pardo, D. Baldomir, and J. Rivas, Phys. Rev. B **78**, 054404 (2008).

[6] L. Liang, S. Qiao, S. Du, S. Zhang, J. Wu, and Z. Liu, Phys. Rev. Mater. **2**, 114409 (2018).

[7] E. Sullivan, J. Hadermann, and C. Greaves, J. Solid State Chem. **184**, 649 (2011).

[8] W. S. Choi, H. Jeen, J. H. Lee, S. S. A. Seo, V. R. Cooper, K. M. Rabe, and H. N. Lee, Phys. Rev. Lett. **111**, 097401 (2013).

[9] F. Saib, B. Bellal, and M. Trari, Mater. Sci. Semicond. Process. **63**, 122 (2017).

[10] S. A. Chambers, T. C. Droubay, C. M. Wang, K. M. Rosso, S. M. Heald, D. A. Schwartz, K. R. Kittilstved, and D. R. Gamelin, Mater. Today **9**, 28 (2006).

[11] S. Ning, P. Zhan, Q. Xie, W. Wang, and Z. Zhang, J. Mater. Sci. Technol. **31**, 969 (2015).

[12] S. Chen, A. Walsh, X.-G. Gong, and S.-H. Wei, Adv. Mater. **25**, 1522 (2013).

[13] P. Erhart, A. Klein, and K. Albe, Phys. Rev. B **72**, 085213 (2005).

[14] S. Komatsuda, W. Sato, and Y. Ohkubo, J. Appl. Phys. **116**, 183502 (2014).

[15] J. Rodriguez, J. M. Gonzalez-Calbet, J. C. Grenier, J. Pannetier, and M. Anne, Solid State Commun. **62**, 231 (1987).

[16] G. H. Jonker and J. H. Van Santen, Physica **19**, 120 (1953).

[17] H. Jeen, Z. Bi, W. S. Choi, M. F. Chisholm, C. A. Bridges, M. P. Paranthaman, and H. N. Lee, Adv. Mater. **25**, 6459 (2013).

[18] C. Mitra, T. Meyer, H. N. Lee, and F. A. Reboredo, J. Chem. Phys. **141**, 084710 (2014).

[19] H. Jeen, W. S. Choi, M. D. Biegalski, C. M. Folkman, I-C. Tung, D. D. Fong, J. W. Freeland, D. Shin, H. Ohta, M. F. Chisholm, and H. N. Lee, Nat. Mater. **12**, 1057 (2013).

[20] M. D. Pashley, Phys. Rev. B **40**, 10481 (1989).

[21] J. Xu, L.-F. Xu, Z.-Z. Li, J.-T. Wang, Z.-S. Lin, K. Liu, Y.-G. Cao, and A. Selloni, Phys. Rev. Appl. **5**, 064001 (2016).

[22] R. Rizk, P. de Mierry, D. Ballutaud, M. Aucouturier, and D. Mathiot, Phys. Rev. B **44**, 6141 (1991).

[23] A. Khare, J. Lee, J. Park, G.-Y. Kim, S.-Y. Choi, T. Katase, S. Roh, T. S. Yoo, J. Hwang, H. Ohta, J. Son, and W. S. Choi, ACS Appl. Mater. Interfaces **10**, 4831 (2018).
[24] G. Kresse and J. Furthmüller, Comput. Mater. Sci. **6**, 15 (1996).
[25] G. Kresse and J. Furthmüller, Phys. Rev. B **54**, 11169 (1996).
[26] J. P. Perdew, K. Burke, and M. Ernzerhof, Phys. Rev. Lett. **77**, 3865 (1996); **78**, 1396(E) (1997).
[27] P. E. Blöchl, Phys. Rev. B **50**, 17953 (1994).
[28] G. Kresse and D. Joubert, Phys. Rev. B **59**, 1758 (1999).
[29] J. Hubbard, Proc. R. Soc. A **276**, 238 (1963).
[30] S. L. Dudarev, G. A. Botton, S. Y. Savrasov, C. J. Humphreys, and A. P. Sutton, Phys. Rev. B **57**, 1505 (1998).
[31] H. A. Jahn and E. Teller, Proc. R. Soc. A **161**, 220 (1937).
[32] J. B. Goodenough and A. L. Loeb, Phys. Rev. **98**, 391 (1955).
[33] S. A. Gold, Low-temperature fuel cell technology for green energy, in *Handbook of Climate Change Mitigation*, edited by W.-Y. Chen, J. Seiner, T. Suzuki, and M. Lackner (Springer US, New York, 2012), pp. 1657–1702.
[34] A. M. Glazer, Acta Crystallogr. Sect. B **28**, 3384 (1972).
[35] G. M. Dalpian, Y. Yan, and S.-H. Wei, Appl. Phys. Lett. **89**, 011907 (2006).
[36] G. M. Dalpian and S.-H. Wei, Phys. Status Solidi B **243**, 2170 (2006).
[37] I. Dzyaloshinsky, J. Phys. Chem. Solids **4**, 241 (1958).
[38] T. Moriya, Phys. Rev. **120**, 91 (1960).